Materials Chemistry and Physics 312 (2024) 128623

Contents lists available at ScienceDirect

Materials Chemistry and Physics

journal homepage: www.elsevier.com/locate/matchemphys

Step by step optimization of luminescence thermometry in $MgTiO_3:Cr^{3+}$, Nd^{3+}@SiO_2 nanoparticles towards bioapplications

Wojciech M. Piotrowski [a,**], Maja Szymczak [a], Emma Martín Rodríguez [b], Riccardo Marin [c], Marta Henklewska [d], Błażej Poźniak [d], Miroslav Dramićanin [e], Lukasz Marciniak [a,*]

[a] Institute of Low Temperature and Structure Research, Polish Academy of Sciences, Okólna 2, 50-422, Wroclaw, Poland
[b] Nanomaterials for Bioimaging Group (nanoBIG), Departamento de Física Aplicada, Facultad de Ciencias, Universidad Autónoma de Madrid, Madrid, Spain
[c] Nanomaterials for Bioimaging Group (nanoBIG), Departamento de Física de Materiales, Facultad de Ciencias, Universidad Autónoma de Madrid, Madrid, Spain
[d] Department of Pharmacology and Toxicology, Faculty of Veterinary Medicine, Wrocław University of Environmental and Life Sciences, ul. Norwida 25, 50-375, Wrocław, Poland
[e] Center of Excellence for Photoconversion, Vinča Institute of Nuclear Sciences – National Institute of the Republic of Serbia, University of Belgrade, P.O. Box 522, Belgrade, 11001, Serbia

HIGHLIGHTS

- New type of biocompatible luminescent thermometer was presented.
- Thermometer operates in the ratiometric and lifetime approaches.
- The process of optimization of thermometric performance of thermometer was presented.
- The deposition of a SiO_2 shell on a $MgTiO_3:Cr^{3+},Nd^{3+}$ slightly elongates the lifetime.
- Low cytotoxicity of the obtained materials was confirmed.

ARTICLE INFO

Keywords:
Magnesium titanate
Decay
Emission
Ti^{3+} ions stabilization
Silica-coated nanoparticles
Cytotoxicity

ABSTRACT

The increasing popularity of luminescent nanothermometry in recent years can be attributed to its application potential in biomedicine. In response to this need, we describe a biocompatible bimodal luminescent thermometer that operates in ratiometric and luminescence lifetime modes based on particles of $MgTiO_3:Cr^{3+}$, Nd^{3+}@SiO_2. The introduction of Cr^{3+} and Nd^{3+} dopants enabled the luminescence of Ti^{3+} ions to be observed, and the difference in the thermal quenching rates of Cr^{3+} ($^4T_2 \rightarrow {}^4A_2$), Ti^{3+} ($^2T_2 \rightarrow {}^2E$) and Nd^{3+} ($^4F_{3/2} \rightarrow {}^4I_{11/2}$) ions enabled the ratiometric thermometers. The highest sensitivity reaching $S_R = 1.00\%K^{-1}$ was obtained for $MgTiO_3$:0.1 % Cr^{3+}, 0.1 % Nd^{3+} at 203 K. The shortening of the lifetime of the $^4T_2$ level of Cr^{3+} ions associated with its thermal depopulation allows to develop a lifetime-based thermometer with a relative sensitivity reaching $0.85–1.18\%K^{-1}$ in the physiological temperature range. The deposition of a SiO_2 shell on a $MgTiO_3:Cr^{3+},Nd^{3+}$ did not introduce significant changes in the shape of the emission spectrum and slightly elongates the lifetime by reducing the probability of surface-related nonradiative processes. More importantly, the thermometric performance of this luminescence thermometer was preserved. The low cytotoxicity of the obtained materials underlines their potential in bioapplications of the described luminescent thermometers.

1. Introduction

Thermal sensing and thermal imaging in biological environments have been found in recent years to be encouraging application fields for the use of luminescence thermometry techniques [1–5]. The temperature readout plays a key role as a diagnostic tool in the detection of inflammation and can also be used for real-time monitoring of hyperthermia treatments [6–8]. Among luminescent thermometers, inorganic

* Corresponding author.
** Corresponding author.
E-mail addresses: w.piotrowski@intibs.pl (W.M. Piotrowski), l.marciniak@intibs.pl (L. Marciniak).

https://doi.org/10.1016/j.matchemphys.2023.128623
Received 3 August 2023; Received in revised form 21 October 2023; Accepted 27 October 2023
Available online 28 October 2023

materials doped with lanthanide (Ln^{3+}) and transition metal (TM) ions have received particular attention in recent years due to their good chemical- and photo-stability [9,10]. However, the design of a material suitable for thermal imaging in a biomedical context requires several optimization steps.

First, suitable host materials and dopants must be selected. The high susceptibility of the luminescence intensity of the transition metal (TM) ions to temperature changes and the ease of modulation of their spectral range of optical response as well as the thermal quenching rate by the modification of the host material is well known. This makes TM-based phosphors especially attractive for application in luminescent thermometry. The best known representative of TM and most extensively studied for this application is Cr^{3+}, whose intense emission can be associated with the $^2E \rightarrow {}^4A_2$ or $^4T_2 \rightarrow {}^4A_2$ electronic transitions. In the former case, the emission is usually observed with a maximum in the range of ~680–780 nm, which can make it difficult to select an excitation wavelength convenient for biological application. However, the $^4T_2 \rightarrow {}^4A_2$ transition can result in an emission band located in the near infrared (NIR) range, within the range of optical biological windows (NIR-I: ~700–950 nm, NIR-II: 1000–1350 nm, NIR-III: 1500–1800 nm). To observe this broad emission band in the spectrum of Cr^{3+} a host material with weak crystal field strength needs to be selected [11–13]. An example of such a material is $MgTiO_3$, where Cr^{3+} ions occupy the relatively large crystallographic sites of Mg^{2+} ions.

The luminescence thermal quenching effect reduces both the intensity of Cr^{3+} emission and the lifetime of the excited state. This allows for the creation of a temporal luminescence thermometer. In contrast, an intensity-based strategy necessitates the use of a reference signal to calculate the ratio of two intensities. The emission bands of lanthanide ions (Ln^{3+}) can be used for this purpose because their emission intensity is less dependent on temperature than that of the Cr^{3+} band. Nd^{3+} stands out among Ln^{3+} ions in terms of biomedical applications due to its efficient emission in NIR-I and NIR-II. In both strategies, dopant concentrations will have a significant impact on thermometric performance, which must be verified thoroughly. Furthermore, the advantage of the chosen host material i.e. $MgTiO_3$ is the possibility of stabilization of Ti^{3+} ions, which further improves the thermal performance of Cr^{3+} luminescence. Stabilization of 6-fold coordinated Ti^{3+} centers has already been confirmed in the case of substitution of A^{2+} sites in $ATiO_3$ titanate host materials (A = Sr, Ca) by Ln^{3+} ions and is associated with the creation of []-Ti^{3+}-O oxygen vacancies (where [] is an oxygen vacancy) [14–16]. In the case of $MgTiO_3$, the location of both Ln^{3+} and Cr^{3+} ions in Mg^{2+} sites allows the stabilization of optically active Ti^{3+} ions, whose excited state can play the role of additional channel of depopulation of Cr^{3+} ions.

When targeting bioapplications, the cytotoxicity of the phosphor is a very important aspect that should be considered. So far, the low toxicity of $MgTiO_3$ nanostructures has been confirmed in the literature [17–19]. However, concerns about long-term cytotoxicity can stem from ion release. To overcome this issue, the phosphor can be encapsulated in an inorganic shell, minimizing ion release. Silica (SiO_2) is often used as a selling material in this scenario due to its ease in the deposition process, high chemical and mechanical stability, low cytotoxicity and the possibility to easily further functionalize its surface. This is expected to ensure safety when introducing nanoparticles under biological conditions without adversely affecting the tissue or cells. However, an important issue is the investigation of the effect of the envelope on the luminescence and thermometric properties of the enveloped materials, which is often an overlooked step in research.

In this work, we report and compare ratiometric and lifetime-based thermometry in $MgTiO_3$ particles co-doped with Cr^{3+} and Nd^{3+} ions. A detailed structural and luminescence characterization is presented to verify the presence of Ti^{3+} ions stabilized by Cr^{3+} ions and thus correctly assign the observed emission bands. Furthermore, the effect of Cr^{3+} and Nd^{3+} ions concentrations on the spectroscopic and thermometric performance was investigated by two thermometric approaches. Finally, the effect of SiO_2 shell on the spectroscopic properties of the coated nanoparticles as well as their cytotoxicity in in vitro measurements using three cell lines was verified.

2. Experimental

2.1. Synthesis of $MgTiO_3$ nanoparticles doped with Cr^{3+} and co-doped with Cr^{3+} and Nd^{3+} ions

The $MgTiO_3$:x% Cr^{3+} (x = 0.1; 0.2; 0.5; 1; 2; 5) and $MgTiO_3$:0.1 % Cr^{3+}, y% Nd^{3+} (y = 0.1; 0.5; 1; 2; 5) nanocrystals were synthesized with a modified Pechini method [20]. The following starting materials were used as reagents without further purification: $Mg(NO_3)_2{\cdot}6H_2O$ (99.999 % purity, Alfa Aesar), $Ti(OC_4H_9)_4$ (99+% purity, Alfa Aesar), 2,4-pentanedione ($C_5H_8O_2$, 99 % purity, Alfa Aesar), $Cr(NO_3)_3{\cdot}9H_2O$ (99.999 % purity, Alfa Aesar), Nd_2O_3 (99.99 % purity, Stanford Materials Corporation), citric acid ($C_6H_8O_7$ >99.5 % purity, Alfa Aesar) and HNO_3 (65 % solution, Avantor). The total amount of Mg^{2+}, Cr^{3+} and Nd^{3+} ions was fixed at 2 mmol since x% Cr^{3+} and y% Nd^{3+} were calculated in respect to the number of Mg^{2+} ions. Firstly, appropriate amount of $Mg(NO_3)_2{\cdot}6H_2O$ and $Cr(NO_3)_3{\cdot}9H_2O$ were dissolved in deionized water and mixed together. In the case of Nd^{3+} co-doped nanocrystals, Nd_2O_3 was dissolved in deionized water with the addition of 2 mL of HNO_3, then recrystallized three times to remove the excess nitrogen and added to the water solution of other nitrates. In a separate beaker 2 mmol of Ti $(OC_4H_9)_4$ was mixed with 2,4-pentanedione in a 1:1 M ratio in order to stabilize the $Ti(OC_4H_9)_4$ solution. The contents of the beaker were gently stirred until a transparent, yellowish solution was obtained, which was then combined with the stabilized nitrate solution. Immediately after that, 24 mmol of an anhydrous citric acid was added to a mixture with the molar ratio of citric acid to all metals set to 6:1. Finally, 24 mmol of PEG-200 was added to the mixture in a 1:1 M ratio with respect to citric acid. The resulting solutions were then dried for 3 days at 363 K until resins were formed. Next, the samples were calcined in porcelain crucibles at 1023 K in air for 8 h. Finally, the obtained powders were ground in an agate mortar.

2.2. Coating of $MgTiO_3$:Cr^{3+}, Nd^{3+} nanoparticles with silica

To obtain silica coated $MgTiO_3$:Cr^{3+}, Nd^{3+} nanoparticles, a modified ultrasound-assisted Stöber method was used [21,22]. The following starting materials were used as reagents: $NH_3{\cdot}H_2O$ (28 % solution, CHEMPUR), tetraethyl orthosilicate (TEOS; ≥99.0 %, Sigma-Aldrich), ethanol (EtOH; 96 % solution; POL-AURA). Specifically, an ethanolic suspension of $MgTiO_3$:Cr^{3+}, Nd^{3+} nanoparticles (30 mg of powder in 23 cm^3 of EtOH) was placed in an ultrasound bath for 2 h, to obtain well-dispersed nanoparticles, without aggregates. After this time, an ammonia solution (0.55 cm^3/7 cm^3 of distilled H_2O) was added to the dispersed nanoparticles and left for 15 min under continuous stirring. Meanwhile, a solution of TEOS in ethanol (0.75 cm^3/7.5 cm^3 EtOH) was prepared and added dropwise. The mixture prepared in this way was again placed in an ultrasound bath for 90 min. After this time, the obtained $MgTiO_3$:Cr^{3+}, Nd^{3+} @SiO_2 were collected by centrifugation (12000 rpm, 5 min) and washed with ethanol 3 times. The purified NPs were redispersed in ethanol or dried, for further analysis.

2.3. Characterization

All of the synthesized materials were examined by X-ray powder diffraction (XRPD) measurements carried out on PANalitycal X'Pert diffractometer, equipped with an Anton Paar TCU 1000 N temperature control unit, using Ni-filtered Cu-K_α radiation (V = 40 kV, I = 30 mA). Rietveld refinement procedure was carried out with PANalytical X'Pert HighScore Plus software. Transmission electron microscope (TEM) images were taken using a FEI TECNAI G2 X-TWIN microscope. Powders were dispersed in methanol with the aid of ultrasounds and deposited on

lacey-type copper grids. The studies were performed with 300 keV parallel beam electron energy. Images were digitally recorded using a Gatan Ultrascan 1000XP camera. The hydrodynamic size of the nanoparticles was determined by dynamic light scattering (DLS), conducted in a Malvern ZetaSizer at room temperature in a polystyrene cuvette, using distilled water as a dispersant.

The emission spectra were measured using the 445 nm excitation lines from a laser diode and a Silver-Nova Super Range TEC spectrometer from Stellarnet (1 nm spectral resolution) as a detector. The low-temperature (83 K) emission and excitation spectra and luminescence decay profiles were recorded using the FLS1000 Fluorescence spectrometer from Edinburgh Instruments with a R5509-72 photomultiplier tube from Hamamatsu in a nitrogen-flow cooled housing as a detector with a 450 W Xenon lamp and 445 nm pulsed work laser diode as an excitation sources. The temperature of the sample was controlled using a THMS 600 heating-cooling stage from Linkam (0.1 K temperature stability and 0.1 K set point resolution).

Thermal dependencies of the luminescence intensity ratio (LIR) were fitted using the Mott–Seitz model (Eq. S1). The average lifetimes of the excited states were calculated with the use of double exponential function according to the procedure described in the Supporting Information (Eq. S2-3).

2.4. Cytotoxicity assessment

The cell lines used in the study included murine fibroblasts 3T3 Swiss Albino, murine macrophages RAW 264.7 (ATCC, Rockville, MD, USA) and canine kidney epithelium line MDCK (Sigma-Aldrich, Steinheim, Germany). All cell lines were cultured in RPMI-1640 medium (Institute of Immunology and Experimental Therapy, Wrocław, Poland) supplemented with 10 % foetal bovine serum (FBS, Sigma, USA), L-glutamine (Sigma, UK) and antibiotics (streptomycin and penicillin, Sigma, Germany). For the cytotoxicity assessment, cells were seeded in 96-well-plates (TTP, Switzerland) at a density of 3×10^3 (3T3, Swiss Albino), 10×10^3 (RAW 264.7) or 2×10^3 (MDCK) cells per well and pre-incubated at 310 K (37 °C) overnight in a humidified atmosphere of 5 % CO_2. After that, dispersions of silica-coated and uncoated $MgTiO_3$:Cr^{3+}, Nd^{3+} were added. The nanoparticles were suspended in 80 % ethanol and bath-sonicated at room temperature for up to 5 min. Next, the stock dispersions were further diluted in sterile 80 % ethanol and dispersions in complete culture medium were prepared so that the concentration of ethanol was 1 % for all nanoparticle dilutions (this concentration was found to be well-tolerated by cells in preliminary experiments). In parallel, the highest nanoparticle concentrations were centrifuged at 30 000 *g* for 1 h and the particle-free supernatants were used as a diluent control (to exclude any possible particle-unrelated effects due to the presence of soluble compounds). Cells were exposed to increasing concentrations (1, 5, 10, 20, 40 μg/ml) of the dispersions for 48 h (5 % CO_2, 310 K). After that, the MTT assay was carried out. This test is based on the enzymatic reduction of the tetrazolium salt MTT [3-(4,5-dimethylthiazol-2-yl)-2,5-diphenyl-tetrazoliumbromide] in living, metabolically active cells. The metabolite, purple-coloured formazan is measured colourimetrically. Preliminary experiments showed no interference of the nanoparticles with MTT in a cell-free system at the concentrations used in this study. After 3.5 h of incubation, cells were lysed with a dedicated buffer (225 mL dimethylformamide, 67.5 g sodium dodecyl sulphate, 275 mL distilled water) and the optical density (OD) was measured after further 24 h using a spectrophotometric microplate reader (Tecan Spark 10 M, Switzerland) at the wavelength of 570 nm (reference 630 nm). The OD of control cells was taken as 100 %. The results were obtained from at least 3 independent experiments and viability values were compared between the control and nanoparticle-exposed cells as well as between both types of nanoparticles using Student's *t*-test ($P \leq 0.05$ was considered statistically significant). Additionally, shortly before MTT addition, pictures were taken using an inverted light microscope coupled with a dedicated camera (Axiovert, Zeiss, Germany).

3. Results and discussion

3.1. Structural and morphological characterization

$MgTiO_3$ crystallizes in a rhombohedral crystal system of the *R*-3 (148) space group. Its structure consists of $(MgO_6)^{10-}$ and $(TiO_6)^{8-}$ octahedra, which form layers in the *ab* plane (Fig. 1a). Due to the presence of two crystallographic sites with the same coordination number (Mg^{2+} and Ti^{4+}), it is of particular interest to consider their substitution mechanism. This is particularly difficult in the case of chromium ions, whose most stable form is Cr^{3+} and occupy only sites with octahedral coordination. For this purpose, a comparison of the effective ionic radii (EIR) of host material ions and dopant ions is most commonly used. In this case, Shannon reports EIR = 72 p.m., 60.5 p.m. and 61.5 p.m. for 6-fold coordinated Mg^{2+}, Ti^{4+} and Cr^{3+} ions, respectively. The smaller difference between the EIR of Ti^{4+} and Cr^{3+} ions clearly suggests that the Ti^{4+} site should be the preferred location of Cr^{3+} ions. However, several works published up to date have discussed the most likely distribution of ions in the $MgTiO_3$ structure after doping it with Cr^{3+} ions [23–25]. Wen-Chen, on the basis of electron paramagnetic resonance (EPR) spectra, reported that Cr^{3+} ions can be located in two sites with distinct surroundings, namely: (A) $Cr^{3+}_{(Mg)}$–$Ti^{4+}_{(Ti)}$ or (B) $Cr^{3+}_{(Mg)}$–$Mg^{2+}_{(Ti)}$ (both cases highlighted in Fig. 1a with a blue glow) [25]. It follows that in case (A), Cr^{3+} ions substitute the crystallographic positions of Mg^{2+} ions, which remain surrounded by Ti^{4+} ions and this situation should be dominant. Case (B), on the other hand, is possible due to the occurrence of the disorder between the Mg^{2+} and Ti^{4+} sublattices in $MgTiO_3$ and implies that Cr^{3+} ions again substitute Mg^{2+} positions, but this also involves the reversed locating of Mg^{2+} ions in Ti^{4+} ion positions. Considering both (A) and (B), the key point is that the Cr^{3+} ions occupy the positions of the larger Mg^{2+} ions rather than the smaller Ti^{4+} ions, which will be also confirmed later in the paper. In the case of Nd^{3+} ions with EIR = 98.3 p.m., they are also expected to substitute Mg^{2+} positions due to the smaller difference between EIR with respect to Ti^{4+} ions. However, by doping $MgTiO_3$ with both Cr^{3+} and Nd^{3+} ions, a charge mismatch is generated. To date, the stabilization of Ti^{3+} ions by Ln^{3+} dopant ions in $SrTiO_3$ and $CaTiO_3$ host materials was confirmed with the use of X-ray photoelectron spectroscopy (XPS) and spectroscopical verification [15,16]. Therefore, the possibility of a similar effect for Nd^{3+} ions in $MgTiO_3$:Cr^{3+}, Nd^{3+} should also be considered here. However, it is possible that a similar situation will occur when the Mg^{2+}-Ti^{4+} pair is replaced by Cr^{3+}-Ti^{3+}. This issue will be discussed later in the paper.

The XRPD patterns of $MgTiO_3$:x% Cr^{3+} nanoparticles have been compared with the reference pattern (ICSD 55285) to verify their phase purity (Fig. 1b). It was found that obtained patterns for $MgTiO_3$:x% Cr^{3+} (where x = 0.1. 0.2 and 0.5) correspond well with reference data. However, additional diffraction reflections were noted for x = 1, 2 and 5. These could be assigned to the impurities of Cr_2MgO_4 (ICSD 250576) and Cr_2O_3 (ICSD 130952). Thus, samples with concentrations higher than 0.5 % of Cr^{3+} ions were not further considered in this work. XRPD patterns of $MgTiO_3$:0.1 % Cr^{3+}, y% Nd^{3+} nanoparticles were also analyzed (Fig. S1). In this case, samples with Nd^{3+} concentration in the range 0.1%–2% do not indicate the presence of a second phase. However, for $MgTiO_3$:0.1 % Cr^{3+}, 5 % Nd^{3+} additional reflections were observed in the diffractograms at 18.18° and 25.53°, which probably correspond to $NdTiO_3$ (ICSD 82008). Therefore, phosphors co-doped maximally with 2 % of Nd^{3+} ions will be included in the following discussion. To investigate the effect of dopants on the unit cell parameters, a Rietveld refinement of the diffractograms was performed (Table S1, Fig. S2). For $MgTiO_3$ singly doped with Cr^{3+}, both *a* and *c* unit cell parameters gradually decrease with an increase of Cr^{3+} concentration (Fig. S3). This observation may suggest that the preferred crystallographic site for Cr^{3+} ions is Mg^{2+} one, since the unit cell shrinkage

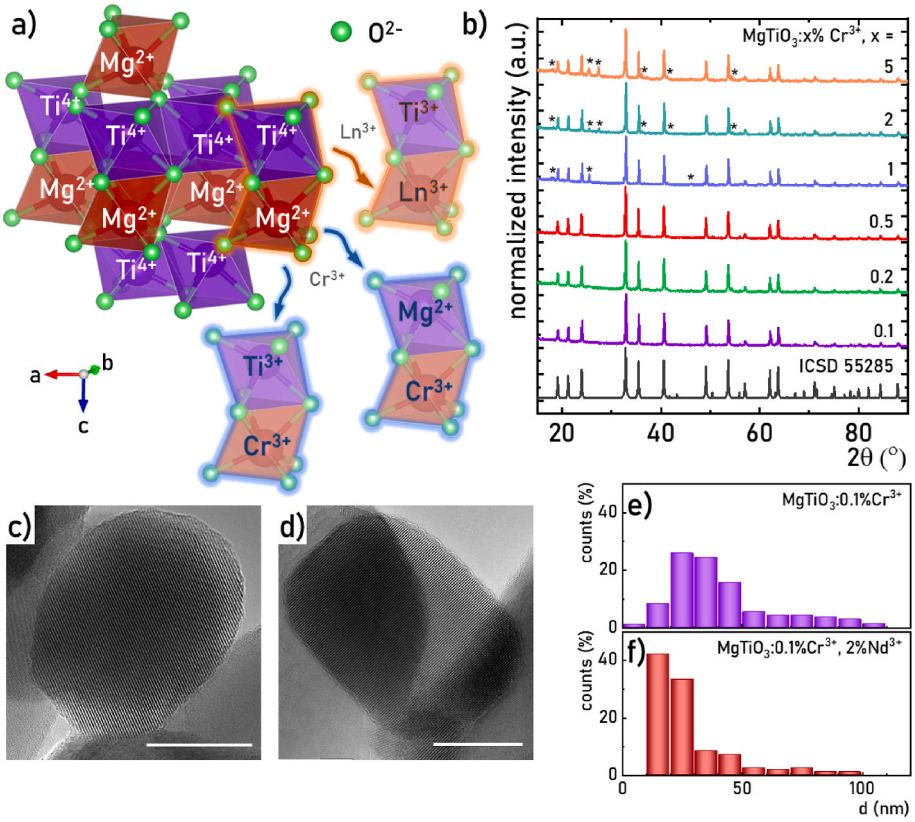

Fig. 1. Crystal structure of half $MgTiO_3$ unit cell – a); X-ray diffraction patterns of $MgTiO_3$ doped with different Cr^{3+} concentration (reflections of the additional phase marked by asterisk) – b); the representative TEM images of $MgTiO_3$:0.1 % Cr^{3+} (scale bar: 20 nm) – c) and $MgTiO_3$:0.1 % Cr^{3+}, 2 % Nd^{3+} (scale bar: 20 nm) – d); particle size distributions for $MgTiO_3$:0.1 % Cr^{3+} – e) and $MgTiO_3$:0.1 % Cr^{3+}, 2 % Nd^{3+} – f).

should be the result of a replacement of larger ions (in this case Mg^{2+} with EIR = 72 p.m.) by a smaller one (Cr^{3+} with EIR = 61.5 p.m.), which would not be the case if Cr^{3+} was replacing Ti^{4+} ions (EIR = 60.5 p.m.). This is consistent with the substitution mechanism mentioned by Wen-Chen [25]. Therefore, on the basis of the presented results, the localization of Cr^{3+} ions in Mg^{2+} positions should be considered as dominant, but there is no direct confirmation that this is the only mechanism for the localization of Cr^{3+} as dopant in $MgTiO_3$. On the other hand, doping with Nd^{3+} ions leads to an expansion of the unit cell, which is in agreement with the substitution of sites of smaller Mg^{2+} ions by larger Nd^{3+} ions. TEM images have been performed for $MgTiO_3$ doped with 0.1 % Cr^{3+} (Fig. 1c and Fig. S4) and 0.1 % Cr^{3+}, 2 % Nd^{3+} (Fig. 1d and Fig. S5). They suggest that the materials are well crystallized and susceptible to agglomeration. In addition, the particle size distribution was determined (Fig. 1e and f, respectively). In both cases, over 90 % of the volume of the material consists of particles smaller than 100 nm. It was observed that co-doping with Nd^{3+} ions yields smaller particles. Specifically, the average particle sizes were determined to be 40 ± 21 nm and 26 ± 16 nm for $MgTiO_3$:0.1%Cr^{3+} and $MgTiO_3$:0.1%Cr^{3+}, 2%Nd^{3+}, respectively. This may suggest that doping with Nd^{3+} ions with charge mismatch in respect to both ions of host material leads to enhanced defect formation, which inhibits the growth of crystallites.

3.2. Luminescent properties characterization

To understand the spectroscopic properties of $MgTiO_3$:Cr^{3+} materials, a configuration coordinate diagram of Cr^{3+} ions should be analyzed (Fig. 2a). Excitation at 445 nm allows the electron to be transferred from the $^4A_2$ ground state to the higher vibronic components of the $^4T_2$ excited state. This is followed by non-radiative depopulation to the bottom of the $^4T_2$ or ^2E parabolas and then radiative relaxation to the $^4A_2$ ground state, which are manifested by bright emission in the red and near infrared spectral range, respectively. Both transitions are observed in the $MgTiO_3$:0.1 % Cr^{3+} emission spectra, where a sharp emission band at 733.5 nm and a broad emission band with a maximum at 835 nm are present (Fig. 2b). They correspond to spin-forbidden $^2E \rightarrow {}^4A_2$ and spin-allowed $^4T_2 \rightarrow {}^4A_2$ electronic transitions of Cr^{3+}, respectively. However, in the case of $MgTiO_3$:0.1 % Cr^{3+}, an additional sharp emission band at 697 nm with a side band at 713 nm was observed. As presented in previous papers [15,16], in titanates with structure $X^{2+}Ti^{4+}O_3$ it is possible to stabilize the optical centers of Ti^{3+} ions by co-doping with Ln^{3+} ions, locally forming Ln^{3+}-Ti^{3+} pairs. Therefore, it has been verified that in $MgTiO_3$ doped with 1 % of La^{3+} ions (that is optically inactive), the luminescence of Ti^{3+} was observed as a sharp band with side band located in the same spectral range as the previously unassigned emission bands detected for $MgTiO_3$:0.1 % Cr^{3+}. Therefore, it should be inferred that doping with Cr^{3+} ions also allows for the stabilization of Ti^{3+} ions, similarly to La^{3+} ions. According to the energy diagram in Fig. 2a, the use of λ_{exc} = 445 nm allows also for the excitation of electrons from O^{2-} ligands to Ti^{4+} ions via charge transfer (CT), followed by nonradiative relaxation to the bottom of ^2E parabola of Ti^{3+} ions and eventual radiative depopulation to $^2T_2$ ground state, resulting in an emission band at 697 nm. Comparing the emission spectra of $MgTiO_3$ doped with different concentrations of Cr^{3+} ions, one can see that the contribution of Ti^{3+} emission associated with the $^2E \rightarrow {}^2T_2$ electronic transition decreases sharply with the change of Cr^{3+} content from 0.1 % to 0.2 % (Fig. 2c). To further confirm the presence of emission originating from two different optical centers, excitation spectra of the $MgTiO_3$:Cr^{3+} for λ_{em} = 697 nm and λ_{em} = 835 nm are shown in Fig. 2d). It can be clearly seen that the broad band around 340 nm (~29 410 cm^{-1}) consists of an overlapping bands, corresponding to $^4A_2 \rightarrow {}^4T_1$ transition of Cr^{3+} ions and CT($O^{2-} \rightarrow Ti^{4+}$), respectively.

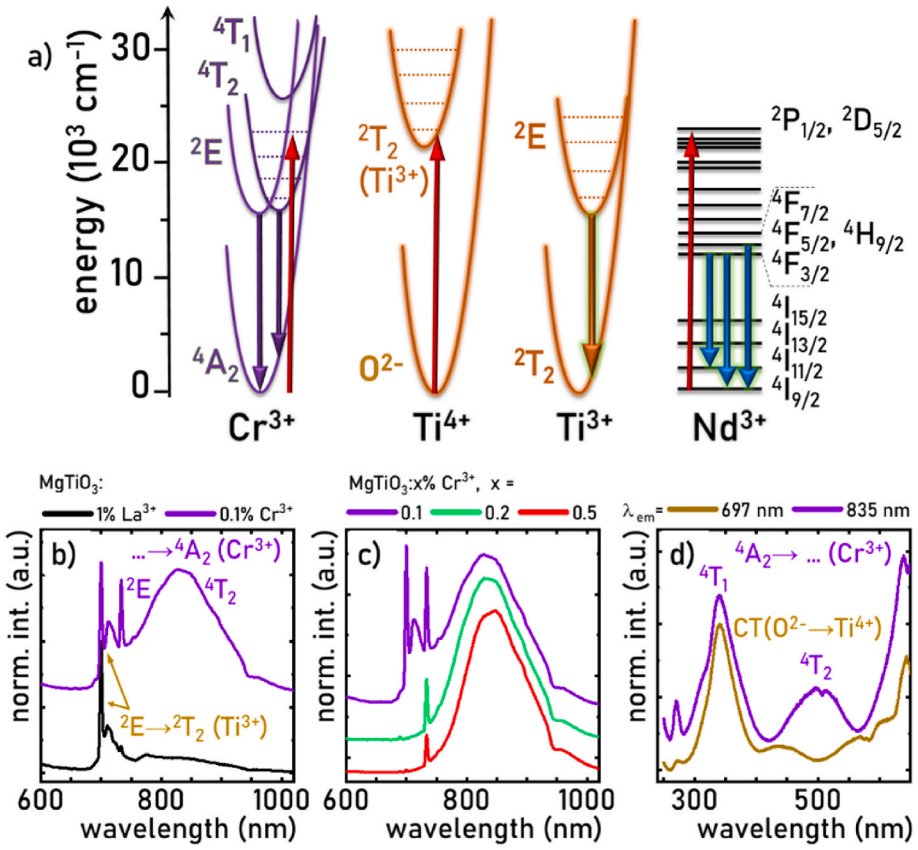

Fig. 2. The simplified configurational coordinate diagram for Cr^{3+}, Ti^{3+} and Nd^{3+} ions – a); comparison of emission spectra (λ_{exc} = 400 nm) for $MgTiO_3$ doped with 1 % La^{3+} and doped with 0.1 % Cr^{3+} ions performed at low temperature (83 K) – b); the influence of Cr^{3+} concentration on emission spectra of $MgTiO_3$:x% Cr^{3+} materials (83K, λ_{exc} = 445 nm) – c); comparison of excitation spectra for λ_{em} = 697 nm and λ_{em} = 835 nm (83 K) in $MgTiO_3$:0.1 % Cr^{3+} phosphor – d).

Additionally, for λ_{em} = 835 nm another broad band with a maximum at 504 nm (~19840 cm^{-1}) was found, which is not present in the excitation spectrum for λ_{em} = 697 nm and corresponds to $^4A_2 \rightarrow ^4T_2$ electronic transition of Cr^{3+} ions. A similar shape of excitation spectra was obtained for $MgTiO_3$:0.5 % Cr^{3+} (Fig. S6). However, due to the slight shift of the excitation band maxima, a crystal field parameter for Cr^{3+} ions was calculated from Eq. S4–S6. The results summarized in Table S2 indicate that the Dq/B parameter grows from 1.86 to 2.04 as the concentration of Cr^{3+} ions changes from 0.1 % to 0.5 %. This is consistent with the previously presented effect of Cr^{3+} ions concentration on shrinking unit cell parameters, since a smaller unit cell size should lead to higher crystal field strength. On the other hand, one can find in Fig. 2c) that this is inconsistent with a shift of the $^4T_2 \rightarrow ^4A_2$ band maximum of Cr^{3+} ions from 830 nm to 845 nm for 0.1 % and 0.5 % Cr^{3+}, respectively. However, a comparison of the shape of the mentioned emission spectra with that of $MgTiO_3$:1 % La^{3+} may suggest that the broad bands associated with the subsequent Ti^{3+} vibronic states with local maxima at 775 nm and 830 nm, overlap spectrally with the $^4T_2 \rightarrow ^4A_2$ emission band for $MgTiO_3$:0.1 % Cr^{3+}, which is no longer observable for $MgTiO_3$:0.5 % Cr^{3+}, generating an error in the attributing of the actual Cr^{3+} broad band maximum.

As further confirmation of the presence and stabilization of Ti^{3+} ions in doped $MgTiO_3$, emission and excitation spectra for $Ba_xMg_{1-x}TiO_3$ structures were analyzed (Figs. S7–9). This topic is further discussed in the Supporting Information.

3.3. *Thermometric properties of Cr^{3+} doped and Cr^{3+} and Nd^{3+} co-doped systems*

The correct assignment of emission bands to optical centers in the $MgTiO_3$:Cr^{3+} emission spectra can also be facilitated by comparing their thermal evolution (Fig. S10). The different quenching rates of the bands located at 697 nm and 713 nm, corresponding to Ti^{3+} emission, and 734 nm and 835 nm, corresponding to Cr^{3+} emission can be clearly seen. Moreover, different quenching rates of Cr^{3+} emission originating from the ^2E and $^4T_2$ levels can also be observed. To allow a quantitative comparison of their characteristics as a function of temperature, the thermal evolution of $^4T_2 \rightarrow ^4A_2$ and $^2E \rightarrow ^4A_2$ emission bands is shown in Figs. S11a–b. In the case of the $^4T_2 \rightarrow ^4A_2$ broad band, the thermal evolution of signal intensity proved to be barely dependent of Cr^{3+} concentration. It decreases slowly from 83 to 143 K reaching ~94 % of the initial intensity. Above this value, the intensity is markedly quenched, at a rate that is faster with increasing Cr^{3+} concentration. Therefore, it is possible to compare the $T_{1/2}$ parameter, defined as the temperature at which the intensity reaches a 50 % of the initial value. $T_{1/2}$ equals 331 K, 295 K and 213 K for 0.1 %, 0.2 % and 0.5 % Cr^{3+}, respectively. Nevertheless, a complete quenching of the emission occurs at ~483 K for all considered concentrations. On the other hand, the ^2E emission intensity decreases rapidly already from 83 K. At 143 K, it reaches 74–81 % of the initial value. It can be seen that in the 83–323 K range the quenching rates of 0.2 % and 0.5 % Cr^{3+} co-doped samples are slightly higher than that of the 0.1 % Cr^{3+} counterpart. Besides, the shape of the thermal evolution of ^2E emission is barely dependent on Cr^{3+} concentration. $T_{1/2}$ equals 243–263 K, while at around 403 K the signal is ~12 % of the initial value. The different thermal quenching rates encourage the determination of the luminescence intensity ratio (LIR) as follows:

$$LIR_1 = \frac{\int_{790\ nm}^{899\ nm} I\left({}^4T_2 \rightarrow {}^4A_2\right)\left[Cr^{3+}\right]d\lambda}{\int_{731\ nm}^{736\ nm} I\left({}^2E \rightarrow {}^4A_2\right)\left[Cr^{3+}\right]d\lambda} \quad \text{(Eq. 1)}$$

The resulting thermal evolution of LIR_1 is shown in Fig. S12a. For all Cr^{3+} concentrations the LIR value initially increases, but its maximum value and the temperature at which it is reached decrease as the concentration of Cr^{3+} ions increases. Thus, $LIR_1 = 1.57$ at 303 K, $LIR_1 = 1.37$ at 183 K and $LIR_1 = 1.25$ at 143 K were obtained for 0.1 %, 0.2 % and 0.5 % Cr^{3+}, respectively. Above these values, the monotonicity of the LIR_1 changes and decreases up to ~460 K. To verify the influence of Cr^{3+} concentration on thermal changes of LIR_1 values, the relative sensitivity S_R was calculated according to the following formula (Eq. 2):

$$S_R = \frac{1}{LIR}\frac{\Delta LIR}{\Delta T} \times 100\% \quad \text{(Eq. 2)}$$

where and ΔLIR represents the change of LIR for the ΔT change of temperature. The obtained S_R results were plotted in Fig. S12b). Firstly, in the temperature range from 83 K to even 291 K negative S_R values were obtained, which are due to the inverse monotonicity of the LIR in respect to the rest of the temperature range. Nevertheless, in the range of 105–114 K the largest S_R values were found to be enhanced with increasing Cr^{3+} concentration and reached $-0.30\%K^{-1}$, $-0.43\%K^{-1}$ and $-0.63\%K^{-1}$ for 0.1 %, 0.2 % and 0.5 % Cr^{3+}, respectively. Besides, the highest S_R values were obtained as follows: $S_R = 0.97\%K^{-1}$ at 450 K, $S_R = 0.65\%K^{-1}$ at 490 K and $S_R = 0.77\%K^{-1}$ at 218 K for 0.1 %, 0.2 % and 0.5 % Cr^{3+}, respectively. Therefore, the $MgTiO_3$:0.1 % Cr^{3+} seems the most encouraging for a potential application. However, to improve the thermometric properties of this luminescent thermometer it was decided to co-dope this material with Nd^{3+} ions. As shown in the energy diagram in Fig. 2a), the use of $\lambda_{exc} = 445$ nm also allows the excitation of Nd^{3+} ions directly through $^2P_{1/2}$, $^2D_{5/2}$ mixed excited levels. This is followed by the nonradiative depopulation to $^4F_{5/2}$, $^4H_{9/2}$ or $^4F_{3/2}$ excited states, from which the emission can be observed. Indeed, the presence of Nd^{3+} bands was confirmed by the comparison of emission spectra of $MgTiO_3$:0.1 % Cr^{3+}, y% Nd^{3+} for y>0.5 % at 83 K (Fig. 4a). These bands are even more evident when comparing the emission spectra at higher temperature (463 K), when the signal from Cr^{3+} emission decreases, revealing the spectral overlap with the Nd^{3+} bands (Fig. S13). It is noteworthy that the Nd^{3+} ions emission bands are much broader than in previously studied materials and which makes impossible to separate the Stark components of the band. In the case of $MgTiO_3$, this shape of the emission bands is the result of the low local symmetry of the crystallographic site occupied by the Nd^{3+} ions. Due to the low local symmetry of Nd^{3+} sites, the presence of Nd^{3+} ions, regardless of their concentration, slightly affects the shape of the broad excitation bands of Cr^{3+} ions (Fig. S14). Another strand worth mentioning in the shape of the emission spectra of $MgTiO_3$ co-doped with Cr^{3+} and Nd^{3+} ions is the presence of bands associated with the $^2E \rightarrow {}^2T_2$ transition of Ti^{3+} ions (Fig. S15). Comparing the emission spectra for $MgTiO_3$:0.1 % Cr^{3+} and $MgTiO_3$:0.1 % Cr^{3+}, 0.1 % Nd^{3+}, which were normalized to the $^4T_2 \rightarrow {}^4A_2$ emission band, it can be seen that the $^2E \rightarrow {}^2T_2$ vibronic band is about 310 % more intense after co-doping with Nd^{3+} ions. This may suggest that the stabilization of Ti^{3+} ions with Nd^{3+} ions is more efficient than with Cr^{3+}, but in this role the influence of Nd^{3+} and Cr^{3+} ions on Ti^{3+} stabilization add up. Next, Fig. 4b) and Fig. S16 show the thermal evolution of the emission spectra of $MgTiO_3$:0.1 % Cr^{3+}, y% Nd^{3+} materials. Similarly to the emission spectra for $MgTiO_3$:Cr^{3+}, the emission signal coming from several optical centers provides different rates of intensity quenching, depending on the wavelength. From several possibilities, two spectral ranges were found to be the most promising: 1) the one corresponding to the Ti^{3+} emission band associated with the $^2E \rightarrow {}^2T_2$ transition (Fig. 3c) and 2) the other with the spectrally

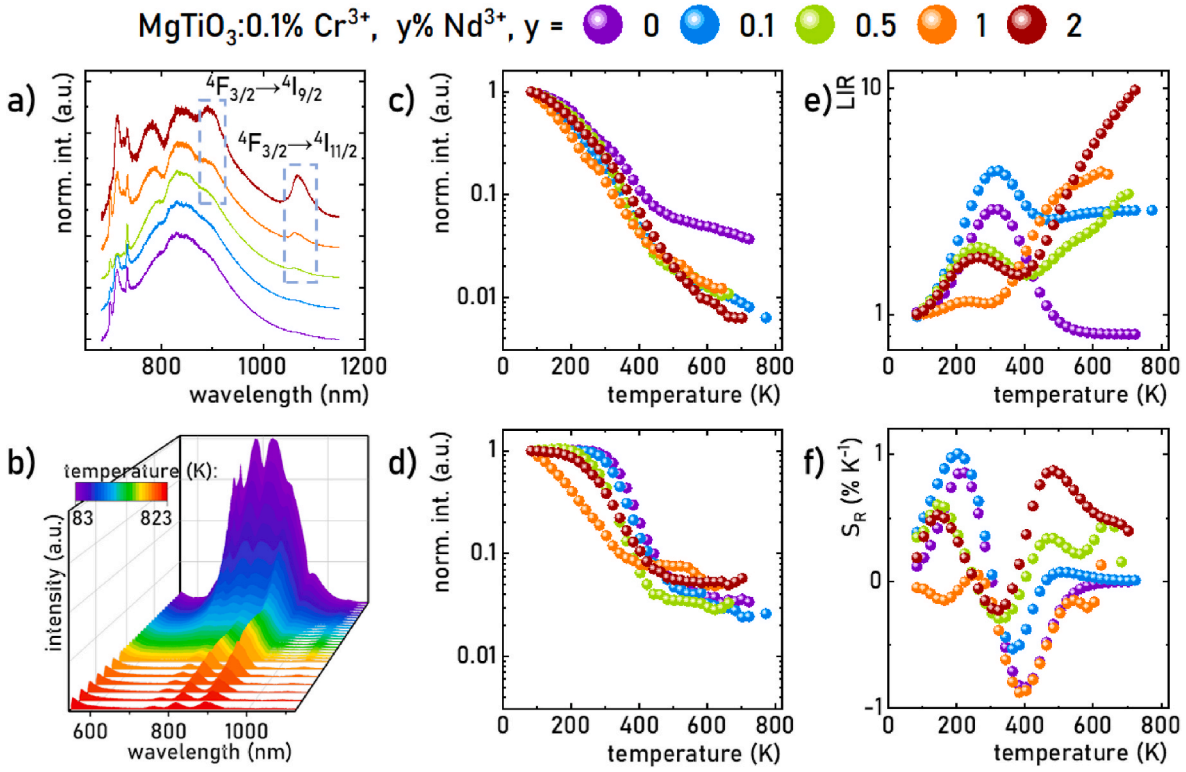

Fig. 3. Influence of Nd^{3+} concentration on the emission spectra of $MgTiO_3$:0.1 % Cr^{3+}, y% Nd^{3+} materials (83K, $\lambda_{exc} = 445$ nm) – a); thermal evolution of emission spectra of $MgTiO_3$:0.1 % Cr^{3+}, 1 % Nd^{3+} phosphor – b); influence of Nd^{3+} concentration on thermal evolution of $^2E \rightarrow {}^2T_2$ (Ti^{3+}) emission band – c); $^4T_2 \rightarrow {}^4A_2$ (Cr^{3+}) + $^4F_{3/2} \rightarrow {}^4I_{9/2}$ (Nd^{3+}) emission band – d); their LIR – e) and relative sensitivity S_R – f).

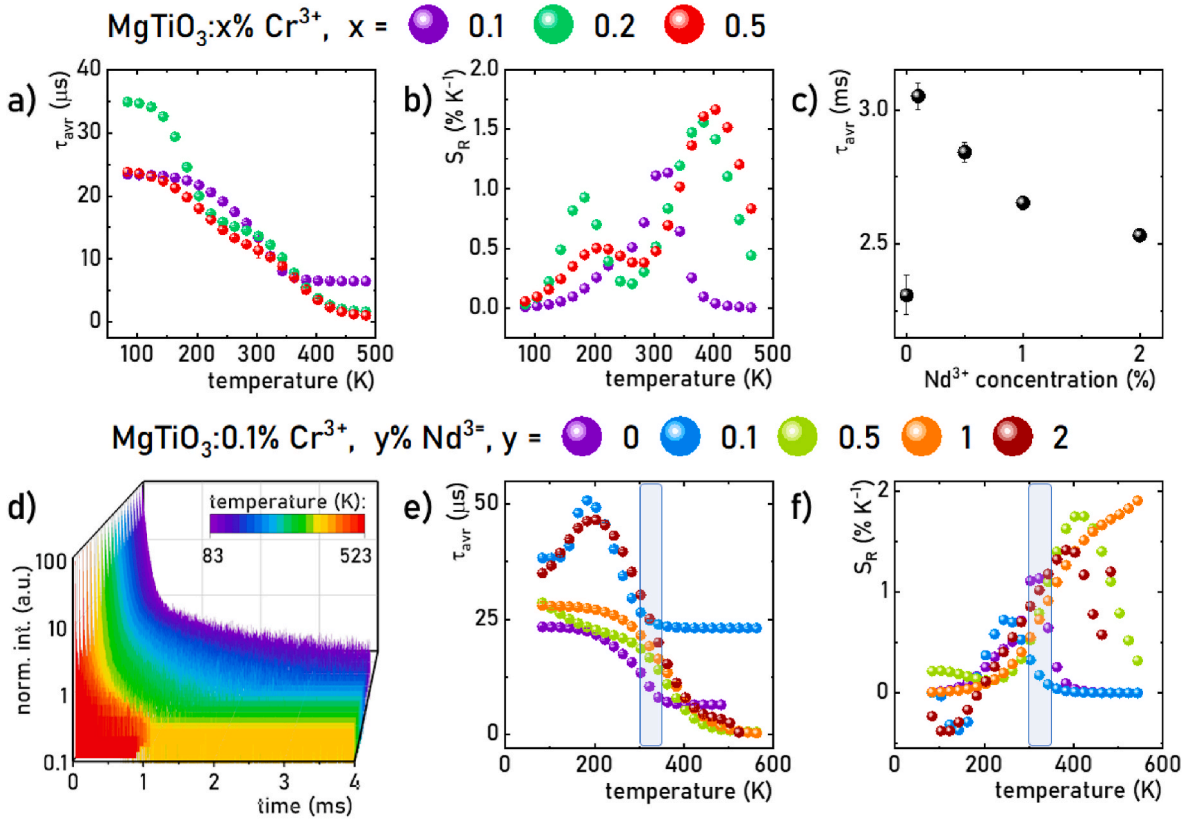

Fig. 4. Thermal evolution of $^4T_2$ excited state lifetime of Cr^{3+} ions – a) and its relative sensitivity for different Cr^{3+} ions concentration in $MgTiO_3$:x% Cr^{3+} materials – b); influence of Nd^{3+} ions concentration on ^2E excited state lifetime of Ti^{3+} ions at 83 K in $MgTiO_3$:0.1 % Cr^{3+}, y% Nd^{3+} – c); thermal evolution of luminescent decay profiles of emission from $^4T_2$ excited state of Cr^{3+} ions in $MgTiO_3$:0.1 % Cr^{3+}, 2 % Nd^{3+} – d); average lifetime – e) and relative sensitivity S_R for $MgTiO_3$:0.1 % Cr^{3+}, y % Nd^{3+} materials – f).

overlapped emission of Cr^{3+} ($^4T_2 \rightarrow {}^4A_2$) and Nd^{3+} ions ($^4F_{3/2} \rightarrow {}^4I_{9/2}$) (Fig. 3d). In the former case, Ti^{3+} emission intensity quasi-linearly decreases from 83 K to 280 K, regardless of Nd^{3+} content. Above this temperature, the signal of all samples co-doped with Nd^{3+} ions quenches faster than the solely doped with Cr^{3+} ions counterpart. It can be seen that in the case of 1 % Nd^{3+}, the intensity of the signal decreases slightly faster with a value of $T_{1/2} = 171$ K in comparison with $T_{1/2}$ values in the range 198–222 K achieved for other concentrations. Then, above ~500 K the emission signal remains below 2 % of the initial value. As a result, it can be concluded that the quenching rate of Ti^{3+} ions is not dependent on the presence and content of Nd^{3+} ions, despite the different contributions to the shape of the emission spectra. On the other hand, Fig. 4d shows a noticeable influence of Nd^{3+} content on the thermal evolution of the intensity signal in the spectral range of the overlapped emission bands of Cr^{3+} ($^4T_2 \rightarrow {}^4A_2$) and Nd^{3+} ($^4F_{3/2} \rightarrow {}^4I_{9/2}$). Firstly, it can be seen that the temperature range, in which the signal remains almost constant shortens. For 0.1 % and 0.5 % Nd^{3+} intensity at 243 K and 203 K is 99 % of the initial value, respectively, in comparison with 263 K for 0 % Nd^{3+}. Above this temperature, gradual thermal quenching occurs. Similar to LIR_1, the different thermal quenching rate of the two spectral ranges selected from the emission spectra of $MgTiO_3$:0.1 % Cr^{3+}, y% Nd^{3+} ions is encouraging for the calculation of the LIR_2 parameter, as follows:

$$LIR_2 = \frac{\int_{950\ nm}^{967\ nm} I\left(\left(^4T_2 \rightarrow {}^4A_2\right)\left[Cr^{3+}\right] + \left(^2F_{9/2} \rightarrow {}^4I_{9/2}\right)\left[Nd^{3+}\right]\right) d\lambda}{\int_{710\ nm}^{717\ nm} I\left(^2E \rightarrow {}^2T_2\right)\left[Ti^{3+}\right] d\lambda} \quad \text{(Eq. 3)}$$

The effect of Nd^{3+} concentration on the thermal dependence of LIR_2 is shown in Fig. 4e. In the case of $MgTiO_3$ solely doped with Cr^{3+} ions, it is noted that LIR_2 increases gradually up to 303 K reaching 292 % of the initial value, and then decreases gradually reaching the same LIR_2 value at 483 K as at 83 K. When co-doped with Nd^{3+}, a similar shape of thermal evolution of LIR_2 can be found, however, the contribution of the Nd^{3+} band in the denominator of LIR_2 is evident in two ways: (I) for 0.1 % Nd^{3+} a rise in LIR_2 to a higher value was obtained, i.e. $LIR_2 = 4.33$ at 323 K, followed by a decrease in LIR_2 for 2.58 at 443 K, which remained more or less constant until 723 K; (II) for higher concentrations (0.5; 1 and 2 %) a continuous increase in LIR_2 was observed from ~400 K onwards. The most dramatic increase in LIR_2 was obtained for the sample with 2 % Nd^{3+}, i.e. from 1.54 to 9.85 in the range 403–723 K. Due to the noticeable effect of Nd^{3+} ions concentration on the temperature range in which the largest changes in LIR_2 value were observed, relative sensitivities were calculated (Fig. 4f). It is evident that the thermal evolution of S_R for all materials follows a similar shape. However, the S_R values that are obtained for the different Nd^{3+} contents vary significantly. It can be seen that the above-mentioned two processes, which are revealed after co-doping with Nd^{3+} ions, are responsible for the improved sensitivity in respect to the Nd^{3+} non co-doped phosphor. Thus, in the first regime the highest $S_R = 1.00\%K^{-1}$ at 203 K was achieved for 0.1 % Nd^{3+} in respect to $S_R = 0.85\%K^{-1}$ at this temperature for Cr^{3+} solely doped counterpart. Then, at around 383 K, $S_R = -0.87\%K^{-1}$ was achieved for 1 % Nd^{3+} in comparison to a similar value of $S_R = -0.85\%K^{-1}$ for the 0 % Nd^{3+} counterpart. As previously mentioned, negative S_R values are indicative of a change in the monotonicity of LIR_2, and their potential use in luminescence thermometry would require a determination of the useful temperature range. Finally, for 2 % Nd^{3+} an $S_R = 0.87\%K^{-1}$ was obtained at 483 K, while above this temperature the S_R value for the solely Cr^{3+} doped sample tends towards zero. Moreover, LIR_2 calculation performed for the heating-cooling cycles also reveals

the thermometric performance of the 2 % Nd^{3+} co-doped materials (Fig. S17). Therefore, luminescence thermometers based on the LIR for $MgTiO_3$ co-doped with Cr^{3+} and Nd^{3+} ions could find a wide range of applications through an appropriate selection of dopant concentrations. However, it should be pointed out that a precisely defined spectral range has to be chosen, which can be a serious practical limitation due to the need to select appropriate optical filters.

Thermal evolution of the luminescence kinetics of Cr^{3+} in Cr^{3+}-doped and Cr^{3+}, Nd^{3+}-co-doped phosphors.

As presented in the case of the emission spectra, the investigated $MgTiO_3$:Cr^{3+} phosphors contain more than one luminescent center, i.e. co-existing Cr^{3+} and Ti^{3+} ions, and also the emission of Cr^{3+} ions can originate from both the ^2E and $^4T_2$ energy levels. Therefore, the effect of the concentration of Cr^{3+} ions followed by Nd^{3+} ions on the lifetimes of excited states needs to be carefully analyzed. Firstly, the thermal evolution of luminescent decay profiles of the $^4T_2$ excited state of Cr^{3+} ions was performed for $MgTiO_3$:Cr^{3+} materials (Fig. S18). The $^4T_2$ excited state was chosen because of its broad and intense emission, for which it will be possible to select measurement parameters that do not to overlap spectrally with other emission bands. Comparing decay profiles for different Cr^{3+} concentrations, it can be noted that in the case of $MgTiO_3$:0.2 % Cr^{3+} (below 200 K) longer decay profiles can be observed comparing to samples doped with 0.1 % and 0.5 % Cr^{3+}. To verify this quantitatively, τ_{avr} was calculated (Fig. 4a). Analyzing the τ_{avr} values, it can be seen that for 0.1 % Cr^{3+} the $\tau_{avr} = 23.8$ μs at 83 K remains almost constant until a temperature of 183 K, above which it gradually shortens to 383 K, where it reaches $\tau_{avr} = 6.67$ μs This value remains constant up to 483 K. It is worth noting the elongation of the lifetime to $\tau_{avr} = 34.9$ μs at 83 K for $MgTiO_3$:0.2 % Cr^{3+}. The lifetimes for 0.1 % Cr^{3+} remain longer than the others up to 203 K, when their τ_{avr} starts to be shorter than 20.0 μs However, in this case the change in quenching rate in the range 243–283K is essential, since it suggests the occurrence of an additional depopulation channel. On this basis, it can be inferred that in the range below 200 K the elongation of lifetimes is related to energy transfer to the ^2E state of Ti^{3+} ions. A similar shape of thermal evolution of τ_{avr} was observed for 0.5 % Cr^{3+} ions, but in this case τ_{avr} at 83 K equals 23.8 μs, which is the same as for the 0.1 % Cr^{3+} counterpart. The shortening of the lifetimes in respect to 0.2 % Cr^{3+} may be due to the shortening of the ^2E state of Ti^{3+} ions as the concentration of both Cr^{3+} and Ti^{3+} ions increases. In order to compare the rate of shortening of decay times depending on Cr^{3+} content, their relative sensitivities were calculated (Fig. 4b). Consistent with the previous observation of one process causing a decrease in τ_{avr} for 0.1 % Cr^{3+} and two processes for 0.2 % and 0.5 % Cr^{3+}, the S_R values are characterized by one or two local maxima, respectively. Thus, the S_{Rmax} for $MgTiO_3$:0.1 % Cr^{3+} is 1.13 % K^{-1} at 323 K. On the other hand, lower local maxima of $S_R = 0.93\%K^{-1}$ at 183 K and $S_R = 0.50\%K^{-1}$ at 203 K were reached for 0.2 % Cr^{3+} and 0.5 % Cr^{3+}, respectively. Above these temperatures, there was a decrease in S_R values in both cases, so that 0.2 % Cr^{3+} reached $S_{Rmax} = 1.55\%K^{-1}$ at 383 K and 0.5 % Cr^{3+} reached $S_{Rmax} = 1.67\%K^{-1}$ at 403 K. Despite the higher S_{Rmax} values obtained for 0.2 % and 0.5 % Cr^{3+} doped samples, for the 0.1 % Cr^{3+} S_R reached higher values in the physiological temperature range. Therefore this sample was selected for further study. When co-doping $MgTiO_3$:Cr^{3+} with Nd^{3+} ions, a marked change in the luminescent decay profiles of ^2E state of Ti^{3+} ions at 83 K was noted, as confirmed by the calculated τ_{avr} values (Fig. S19, Fig. 4c). Importantly, an increase in the lifetimes of Ti^{3+} ions from $\tau_{avr} = 2.31$ ms–3.05 ms was observed for co-doped $MgTiO_3$:0.1 % Cr^{3+} with 0.1 % Nd^{3+} ions. This may suggest that doping with Nd^{3+} ions with charge mismatch and larger EIR in respect to Mg^{2+} ions, leads to the generation of greater lattice distortion in respect to Cr^{3+} ions. As is well known, the local symmetry of a luminescent ion affects the probability of radiative depopulation of the excited state od luminescent ions thus having an impact on their lifetimes. An increase of the local symmetry of the ion and the crystallization degree through the co-doping which leads to the elongation of the luminescence kinetics has been already demonstrated for lanthanide doped [26,27] changes in local symmetry the co-doping of $MgTiO_3$:Cr^{3+} with Nd^{3+} can lead to the observed elongation of the Ti^{3+} lifetime. Similar effect was already observed in $SrTiO_3$:Ln^{3+} [28].

Then, for higher concentrations of Nd^{3+} ions, an expected gradual reduction in the lifetimes of Ti^{3+} ions is observed, up to $\tau_{avr} = 2.53$ ms for 2 % Nd^{3+} ions. The effect of Nd^{3+} concentration was also evaluated for the thermal evolution of Cr^{3+} lifetimes (Fig. 4d and Fig. S20). The calculated τ_{avr} in Fig. 4e confirms the beneficial effect of Nd^{3+} ions on the elongation of Cr^{3+} lifetimes, irrespective of Nd^{3+} concentration. The longest τ_{avr} at 83 K was obtained for 0.1 % Nd^{3+} ions equal to 38.3 μs (~64 % longer than for the solely Cr^{3+} doped counterpart). In this case, up to 183 K there is an increase in lifetimes, reaching 50.9 μs Above this temperature, τ_{avr} decreases until $\tau_{avr} = 23.4$ μs at 363 K. When co-doped with 0.5 % and 1 % of Nd^{3+} ions, $\tau_{avr} =$ ~28.0 μs at 83 K, which is only 20 % higher than the Cr^{3+} solely doped sample. Above 83 K for these two concentrations, no increase in lifetimes was observed either. For concentrations higher than 0.1 % Nd^{3+} above ~220 K, a gradual decrease in τ_{avr} value with increasing temperature can be observed, leading to a value of less than 5 μs after exceeding 443 K. Surprisingly, similar to 0.1 % Nd^{3+}, significant elongation of Cr^{3+} ions lifetimes was obtained for 2 % Nd^{3+}. This may suggest that the concentration of 2 % of Nd^{3+} is sufficient to lead to the greatest lattice distortion affecting the lifetimes of Cr^{3+} ions in respect to other Nd^{3+} concentrations. From 83 to 203 K elongation to 46.6 μs at 203 K and gradual shortening was obtained, similarly to 0.5 % and 1 % Nd^{3+} counterparts. Fig. 4f compares the relative sensitivities calculated for τ_{avr} of $MgTiO_3$:Cr^{3+}, Nd^{3+} materials. The highest values were obtained for 0.5 % Nd^{3+} ions equal to $S_{Rmax} = 1.75\%K^{-1}$ at 413 K, and for 1 % Nd^{3+} the S_R reaches even $1.90\%K^{-1}$ at 543 K. For this reason, co-doping with Nd^{3+} ions should be considered to have a beneficial effect on S_R values. When considering the potential use of phosphors in thermometry operating in the physiological temperature range, it is also worth noting the increase in lifetimes in respect to $MgTiO_3$ solely doped with Cr^{3+} ions, which performed most favorably for samples with 0.5 % and 2 % Nd^{3+} ions. However, of the two materials, the one with 2 % Nd^{3+} achieved S_R values in the range of 0.85–1.18%K^{-1} over 303–343 K in respect to S_R values of less than $0.33\%K^{-1}$ for 0.5 % Nd^{3+} ions. Moreover, heating–cooling cycles performed for $MgTiO_3$:0.1 % Cr^{3+}, 2 % Nd^{3+} confirm a good repeatability in their lifetime-based thermometric performance (Fig. S21). On this basis, the $MgTiO_3$:0.1 % Cr^{3+}, 2 % Nd^{3+} phosphor was selected as the most suitable for further optimization.

3.4. Improving potential of biological application through silica-coating

To improve the application potential of the selected nanoparticles, they were coated with SiO_2 layer using the modified Stöber method, described in detail in the Experimental section. TEM images of SiO_2-coated nanoparticles are shown in Fig. 5a and b and Fig. S22. It can be found that nanoparticles are coated with silica of quasi constant thickness. From the TEM images, the average thickness of the silica shell was determined to be 7 ± 1 nm (Fig. S23). Subsequently, the spectroscopic properties of $MgTiO_3$:0.1 % Cr^{3+}, 2 % Nd^{3+} nanoparticles uncoated and coated with silica were compared. No significant changes in the shape of emission spectra were found (Fig. 5c). Special attention should be paid to the effect of silica coating on the Cr^{3+} excited state lifetimes, conducted in the physiological temperature range 293 K–323 K (Fig. 5d, Fig. S24). At 293 K, a slight increase in τ_{avr} values from 32.2 μs to 32.8 μs for the silica coated sample was observed. A similar trend continues throughout the temperature range, for which an elongation of 0.55 ± 0.16 μs was determined. This phenomenon can be explained by the reduction of the probability of the nonradiative depopulation of the excited state by the surface related quenchers (surface defects, OH molecules attached to the surface etc.) when the SiO_2 is deposited on the $MgTiO_3$:Cr^{3+},Nd^{3+} surface.

Furthermore, to verify the application potential of nanoparticles coated with silica, cytotoxicity assessments were performed.

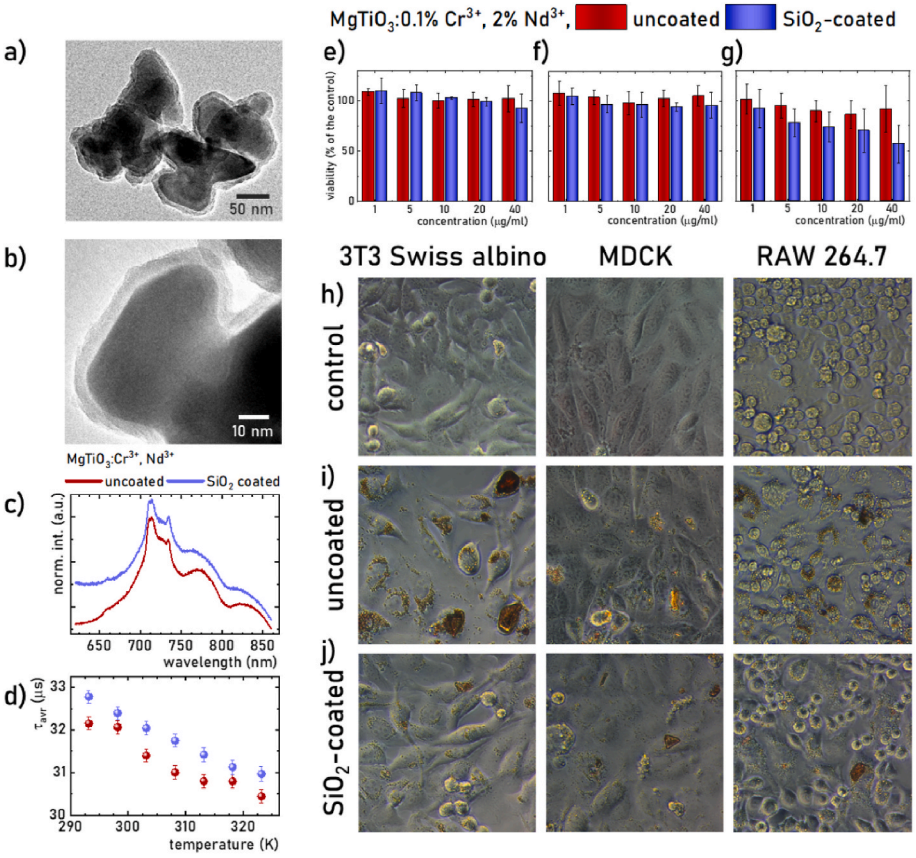

Fig. 5. Representative TEM images of $MgTiO_3$:0.1 % Cr^{3+}, 2 % Nd^{3+} coated with SiO_2 layer – a), b); comparison of emission spectra at 83 K – c) and average lifetimes of $^4T_2$ excited state of Cr^{3+} ions in $MgTiO_3$:0.1 % Cr^{3+}, 2 % Nd^{3+} non-coated and coated with SiO_2 – d); viability assessment (mean ± SD) using MTT assay in three cell lines exposed to uncoated and silica-coated $MgTiO_3$:0.1 % Cr^{3+}, 2 % Nd^{3+} nanoparticles – d), e), f); control fibroblasts (3T3-Swiss albino), kidney epithelium cells (MDCK) and macrophages (RAW 264.7) (magnification 400 ×) – h); the same cell lines exposed to uncoated $MgTiO_3$:0.1 % Cr^{3+}, 2 % Nd^{3+} nanoparticles at a concentration of 40 μg/ml for 48 h (magnification 400 ×) – i); the same cell lines exposed to silica-coated $MgTiO_3$:0.1 % Cr^{3+}, 2 % Nd^{3+} nanoparticles at a concentration of 40 μg/ml for 48 h (magnification 400 ×) – j).

Cytotoxicity tests were carried out on murine fibroblast (3T3-Swiss albino), murine macrophage (RAW 264.7) and Madin-Darby canine kidney (MDCK) cell lines. Cell lines have been selected as an *in vitro* model based on their wide use in toxicity studies as well as the specific functions these types of cells have in the organism. Fibroblasts are the main cellular component of connective tissues and 3T3 fibroblasts are a standard model to screen for cytotoxicity of implants and biomaterials [29,30]. Under *in vivo* conditions, macrophages form the primary line of defense to foreign bodies e.g. particulate matter, implants or biomaterials [31,32]. Thus they are responsible for the distribution and clearance of nanoparticles and their agglomerates. Lastly, the MDCK kidney cell line was chosen as renal elimination is frequently encountered in metal-based nanoparticles and the risk of nephrotoxicity has been reported [33]. The effects of silica-coated and uncoated $MgTiO_3$:Cr^{3+}, Nd^{3+} nanoparticles on cell viability are summarized in Fig. 5e)-g). For the uncoated nanoparticles, no significant cytotoxicity in any cell line was seen up to the maximum concentration of 40 μg/ml. When exposed to the silica-coated nanoparticles, both 3T3 and MDCK cells showed no decrease in viability. In contrast, the macrophage line RAW 264.7 seemed to show a moderate dose-dependent decrease which never exceeded 50 %. These differences, however, were not found to be significant. Particle-free supernatants of both materials were found to be non-toxic to all three cell lines. Visual inspection of the cells exposed for 48 h to both silica-coated and uncoated $MgTiO_3$:Cr^{3+}, Nd^{3+} suggested some degree of particle internalization in 3T3 and RAW 264.7 cells but not in the MDCK cells (Fig. 5h–j). For the 3T3 fibroblasts the main route of particle internalization are different types of endocytosis [34], whereas RAW 264.7 cells are known to be efficient in phagocytosis – a route targeting much larger, micron-sized agglomerates [35]. Since the uptake of nanoparticles was clear in both cell lines it seems that nanoparticles could reach the cellular compartment by both phagocytosis (larger agglomerates) and endocytosis (free particles and small agglomerates). Moreover, the uncoated particles seemed to be internalized to a higher degree as the number of cells loaded with optically dense particles was visibly higher as compared to cells exposed to the silica-coated particles. The perinuclear deposition supports the intracellular localization of the material (and not only physical adsorption on the surface). The increased uptake of uncoated particles may be related to two factors: 1) The dispersion of uncoated $MgTiO_3$:Cr^{3+}, Nd^{3+} nanoparticles was visibly less stable as compared to their coated counterparts leading to faster sedimentation and higher dose delivered directly to cells over time [36], and 2) Silica-coated surface created an interface that was not stimulating cellular uptake to a degree observed with the uncoated $MgTiO_3$:Cr^{3+}, Nd^{3+} nanoparticle surface. Quantitative uptake assessment, however, has not been performed in this study.

Surprisingly, the apparently less internalized silica-coated particles seemed to inhibit cell proliferation in the macrophage cell line to a greater extent than the more internalized uncoated particles. This effect is difficult to explain. It seems not to be related to ion release as both supernatants proved to be non-toxic, moreover, internalized material should be more prone to ion release in the acidic environment of the phagosomes [35,37]. Even if internalized, silica shell would be expected to decrease the release of toxic ions from the particle's core. Apart from the presence of silica shell and stability in the dispersion, these two

materials differed by their hydrodynamic diameters as measured by DLS in a complete cell culture medium. The coated particles showed a single peak with the mean hydrodynamic diameter of 420 ± 100 nm, whereas the uncoated particles were represented by two peaks of smaller (210 ± 40 nm) and larger particles/agglomerates (740 ± 170 nm). This difference, however, also does not seem to explain the concentration-dependent trend in the viability decrease in RAW 264.7 cells. It seems likely that the protective core itself contributes to this selective sensitivity at higher concentrations. Unmodified silica shell will provide negative surface charge to the nanoparticle system and it is known that negatively charged silica nanoparticles are more toxic to RAW 264.7 cells as compared with positively charged ones [38]. This, however, is typically explained by an increased uptake of negatively charged particles.

The nanoparticles under investigation were found to be biocompatible in the applied *in vitro* model of MDCK and 3T3 cells. On the other hand, the results for RAW 264.7 macrophages suggest a risk of some degree of cytotoxicity to phagocytic cells. More quantitative uptake studies are needed to elucidate the precise mechanisms of cell-specific sensitivity to silica-coated particles.

4. Conclusions

The work presents the step by step investigation of luminescent thermometers based on $MgTiO_3:Cr^{3+}$, $Nd^{3+}@SiO_2$ nanoparticles with potential for bioapplications. At first, it was found that both Cr^{3+} and Nd^{3+} lead to the stabilization of Ti^{3+} ions, whose emission is observed for 0.1 % Cr^{3+} solely doped $MgTiO_3$ and Nd^{3+} co-doped materials. Bands of Ti^{3+} ($^2E \rightarrow {}^2T_2$) together with overlapped Cr^{3+} ($^4T_2 \rightarrow {}^4A_2$) and Nd^{3+} ($^4F_{3/2} \rightarrow {}^4I_{9/2}$) were used to verify the thermometric performance of LIR-based approach. Two main temperature ranges with relatively good sensitivity were obtained for this strategy, i.e. around 203 K with the highest $S_R = 1.00\%K^{-1}$ for 0.1 % Nd^{3+} and at 483 K with the representative $S_R = 0.87\%K^{-1}$ for 2 % Nd^{3+}. Subsequently, the investigation of the luminescent decay profiles of emission from $^4T_2$ excited state of Cr^{3+} ions presented that co-doping with Nd^{3+} ions leads to prolonged Cr^{3+} lifetimes, an important advantage reducing temperature determination uncertainty. For this approach, $S_R = 1.75\%K^{-1}$ at 413 K for 0.5 % Nd^{3+} and even $S_{Rmax} = 1.90\%K^{-1}$ at 543 K for 1 % Nd^{3+} were obtained. Finally, $MgTiO_3$:0.1 % Cr^{3+}, 2 % Nd^{3+} phosphor with S_R ranges between 0.85 and $1.18\%K^{-1}$ over 303–343 K was selected for the silica encapsulation and the cytotoxicity measurements with a view to biorelated applications. It was found that the SiO_2 shell does not significantly affect the shape of the emission spectrum, but slightly extends the lifetime, which may be related to a decrease in the probability of surface-related non-radiative processes. The nanoparticles with a silica shell were found to be non-toxic to MDCK and 3T3 cells, although they may adversely affect phagocytic cells.

CRediT authorship contribution statement

Wojciech M. Piotrowski: Methodology, Investigation, Measurements, Visualization, Writing – original draft. **Maja Szymczak:** Methodology, Investigation. **Emma Martín Rodríguez:** Methodology, Investigation. **Riccardo Marin:** Methodology, Investigation, Visualization, Writing – original draft. **Marta Henklewska:** Methodology, Investigation. **Błażej Poźniak:** Methodology, Investigation, Writing – original draft. **Miroslav Dramićanin:** Methodology, Investigation. **Lukasz Marciniak:** Methodology, Investigation, Writing – original draft.

Declaration of competing interest

The authors declare that they have no known competing financial interests or personal relationships that could have appeared to influence the work reported in this paper.

Data availability

Data will be made available on request.

Acknowledgements

The authors thank prof. Daniel Jaque (Universidad Autónoma de Madrid) for his support. WM. P. acknowledges the financial support from the Bekker NAWA Programme BPN/BEK/2021/1/00029 funded by Polish National Agency for Academic Exchange. WM. P. acknowledges also the support from Foundation for Polish Science (FNP) under the START programme.

Appendix A. Supplementary data

Supplementary data to this article can be found online at https://doi.org/10.1016/j.matchemphys.2023.128623.

References

[1] X.D. Wang, O.S. Wolfbeis, R.J. Meier, Luminescent probes and sensors for temperature, Chem. Soc. Rev. 42 (2013) 7834–7869, https://doi.org/10.1039/c3cs60102a.
[2] L. Labrador-Páez, M. Pedroni, A. Speghini, J. García-Solé, P. Haro-González, D. Jaque, Reliability of rare-earth-doped infrared luminescent nanothermometers, Nanoscale 10 (2018) 22319–22328, https://doi.org/10.1039/c8nr07566b.
[3] D. Jaque, F. Vetrone, Luminescence nanothermometry, Nanoscale 4 (2012) 4301–4326, https://doi.org/10.1039/c2nr30764b.
[4] M. Dramićanin, Luminescence: the basics, methods, and instrumentation, in: M.B. T.-L.T. Dramićanin (Ed.), Lumin. Thermom., Woodhead Publishing, 2018, pp. 33–61, https://doi.org/10.1016/b978-0-08-102029-6.00003-8.
[5] M.D. Dramićanin, Trends in luminescence thermometry, J. Appl. Phys. 128 (2020), 40902, https://doi.org/10.1063/5.0014825.
[6] M. Tan, F. Li, N. Cao, H. Li, X. Wang, C. Zhang, D. Jaque, G. Chen, Accurate in vivo nanothermometry through NIR-II lanthanide luminescence lifetime, Small 16 (2020), 2004118, https://doi.org/10.1002/smll.202004118.
[7] J. Morales-Dalmau, C. Vilches, I. De Miguel, V. Sanz, R. Quidant, Optimum morphology of gold nanorods for light-induced hyperthermia, Nanoscale 10 (2018) 2632–2638, https://doi.org/10.1039/c7nr06825e.
[8] E. Ximendes, R. Marin, Y. Shen, D. Ruiz, D. Gómez-Cerezo, P. Rodríguez-Sevilla, J. Lifante, P.X. Viveros-Méndez, F. Gámez, D. García-Soriano, G. Salas, C. Zalbidea, A. Espinosa, A. Benayas, N. García-Carrillo, L. Cussó, M. Desco, F.J. Teran, B. H. Juárez, D. Jaque, Infrared-Emitting multimodal nanostructures for controlled in vivo magnetic hyperthermia, Adv. Mater. 33 (2021), 2100077, https://doi.org/10.1002/adma.202100077.
[9] E. Martín Rodríguez, G. López-Peña, E. Montes, G. Lifante, J. García Solé, D. Jaque, L.A. Diaz-Torres, P. Salas, Persistent luminescence nanothermometers, Appl. Phys. Lett. 111 (2017), 81901, https://doi.org/10.1063/1.4990873.
[10] S.W. Allison, G.T. Gillies, Remote thermometry with thermographic phosphors: instrumentation and applications, Rev. Sci. Instrum. 68 (1997) 2615–2650, https://doi.org/10.1063/1.1148174.
[11] K. Elzbieciak-Piecka, C. Matuszewska, L. Marciniak, Step by step designing of sensitive luminescent nanothermometers based on Cr3+,Nd3+ co-doped La3-: XLuxAl5- yGayO12 nanocrystals, New J. Chem. 43 (2019) 12614–12622, https://doi.org/10.1039/c9nj03167g.
[12] P. Dang, Y. Wei, D. Liu, G. Li, J. Lin, Recent advances in chromium-doped near-infrared luminescent materials: fundamentals, optimization strategies, and applications, Adv. Opt. Mater. 11 (2023), 2201739.
[13] M.G. Brik, C.-G. Ma, Theoretical Spectroscopy of Transition Metal and Rare Earth Ions, 2019, https://doi.org/10.1201/9780429278754.
[14] T. Kubo, H. Nozoye, Surface structure of SrTiO3(1 0 0), Surf. Sci. 542 (2003) 177–191, https://doi.org/10.1016/S0039-6028(03)00998-1.
[15] W. Piotrowski, M. Kuchowicz, M. Dramićanin, L. Marciniak, Lanthanide dopant stabilized Ti3+ state and supersensitive Ti3+ -based multiparametric luminescent thermometer in SrTiO3:Ln3+ (Ln3+ = Lu3+, La3+, Tb3+) nanocrystals, Chem. Eng. J. 428 (2022), 131165.
[16] W.M. Piotrowski, Z. Ristic, M.D. Dramićanin, Marciniak, Modification of the thermometric performance of the lifetime-based luminescent thermometer exploiting Ti3+ emission in SrTiO3 and CaTiO3 by doping with lanthanide ions, J. Alloys Compd. 906 (2022), 164398, https://doi.org/10.1016/j.jallcom.2022.164398.
[17] L. Meng, Z. Ren, W. Zhou, Y. Qu, G. Wang, MgTiO3/MgTi2O5/TiO2 heterogeneous belt-junctions with high photocatalytic hydrogen production activity, Nano Res. 10 (2017) 295–304, https://doi.org/10.1007/s12274-016-1292-6.
[18] X. Wang, J. Cai, Y. Zhang, L. Li, L. Jiang, C. Wang, Heavy metal sorption properties of magnesium titanate mesoporous nanorods, J. Mater. Chem. A 3 (2015) 11796–11800, https://doi.org/10.1039/C5TA02034D.
[19] Y. Suzuki, M. Morimoto, Porous $MgTi_2O_5/MgTiO_3$ composites with narrow pore-size distribution: *in situ* processing and pore structure analysis, J. Ceram. Soc. Japan. 118 (2010) 819–822, https://doi.org/10.2109/jcersj2.118.819.

[20] M.P. Pechini, Method of Preparing Lead and Alkaline Earth Titanates and Niobates and Coating Method Using the Same to Form a Capacitor, 1967.
[21] K. Kniec, K.A. Ledwa, L. Marciniak, Role of SiO2 coating on YAG:V3+,Nd3+ nanoparticles in luminescence thermometry, ACS Appl. Nano Mater. 5 (2022) 8271–8278, https://doi.org/10.1021/acsanm.2c01180.
[22] W. Stöber, A. Fink, E. Bohn, Controlled growth of monodisperse silica spheres in the micron size range, J. Colloid Interface Sci. 26 (1968) 62–69, https://doi.org/10.1016/0021-9797(68)90272-5.
[23] A.F.M.Y. Haider, A. Edgar, ESR study of transition metal ions in magnesium titanate, J. Phys. C Solid State Phys. 13 (1980) 6239, https://doi.org/10.1088/0022-3719/13/33/022.
[24] N. Kuganathan, P. Iyngaran, R. Vovk, A. Chroneos, Defects, dopants and Mg diffusion in MgTiO3, Sci. Rep. 9 (2019) 4394, https://doi.org/10.1038/s41598-019-40878-y.
[25] Z. Wen-Chen, EPR study of two Cr3+ sites in MgTiO3 crystal, J. Phys. Chem. Solid. 55 (1994) 647–650.
[26] Y. Li, C. Liu, P. Zhang, J. Huang, H. Ning, P. Xiao, Y. Hou, L. Jing, M. Gao, Doping lanthanide nanocrystals with non-lanthanide ions to simultaneously enhance up- and down-conversion luminescence, Front. Chem. 8 (2020), https://doi.org/10.3389/fchem.2020.00832.
[27] G.B. Kadri, D. Das, S.K. Gupta, K. Sudarshan, Influence of Li+ co-doping on the luminescence of MgO:Eu3+ nanocrystals: probing asymmetry, energy transfer and defects, Solid State Sci. 105 (2020), 106286.
[28] W. Piotrowski, M. Kuchowicz, M. Dramićanin, L. Marciniak, Lanthanide dopant stabilized Ti3+ state and supersensitive Ti3+ -based multiparametric luminescent thermometer in SrTiO3:Ln3+ (Ln3+ = Lu3+, La3+, Tb3+) nanocrystals, Chem. Eng. J. 428 (2021), 131165, https://doi.org/10.1016/j.cej.2021.131165.
[29] W. Geurtsen, F. Lehmann, W. Spahl, G. Leyhausen, Cytotoxicity of 35 dental resin composite monomers/additives in permanent 3T3 and three human primary fibroblast cultures, J. Biomed. Mater. Res. 41 (1998) 474–480, https://doi.org/10.1002/(SICI)1097-4636(19980905)41:3<474::AID-JBM18>3.0.CO;2-I.
[30] S.K. Bhatia, A.B. Yetter, Correlation of visual in vitro cytotoxicity ratings of biomaterials with quantitative in vitro cell viability measurements, Cell Biol. Toxicol. 24 (2008) 315–319, https://doi.org/10.1007/s10565-007-9040-z.
[31] R. Miyata, S.F. van Eeden, The innate and adaptive immune response induced by alveolar macrophages exposed to ambient particulate matter, Toxicol. Appl. Pharmacol. 257 (2011) 209–226, https://doi.org/10.1016/j.taap.2011.09.007.
[32] H.C. Fischer, T.S. Hauck, A. Gómez-Aristizábal, W.C.W. Chan, Exploring primary liver macrophages for studying quantum dot interactions with biological systems, Adv. Mater. 22 (2010) 2520–2524, https://doi.org/10.1002/adma.200904231.
[33] P. Makhdoumi, H. Karimi, M. Khazaei, Review on metal-based nanoparticles: role of reactive oxygen species in renal toxicity, Chem. Res. Toxicol. 33 (2020) 2503–2514, https://doi.org/10.1021/acs.chemrestox.9b00438.
[34] D. Drescher, G. Orts-Gil, G. Laube, K. Natte, R.W. Veh, W. Österle, J. Kneipp, Toxicity of amorphous silica nanoparticles on eukaryotic cell model is determined by particle agglomeration and serum protein adsorption effects, Anal. Bioanal. Chem. 400 (2011) 1367–1373, https://doi.org/10.1007/s00216-011-4893-7.
[35] X. Liu, N. Huang, H. Li, Q. Jin, J. Ji, Surface and size effects on cell interaction of gold nanoparticles with both phagocytic and nonphagocytic cells, Langmuir 29 (2013) 9138–9148, https://doi.org/10.1021/la401556k.
[36] J.G. Teeguarden, P.M. Hinderliter, G. Orr, B.D. Thrall, J.G. Pounds, Particokinetics in vitro: dosimetry considerations for in vitro nanoparticle toxicity assessments, Toxicol. Sci. 95 (2007) 300–312, https://doi.org/10.1093/toxsci/kfl165.
[37] G. Despras, A.I. Zamaleeva, L. Dardevet, C. Tisseyre, J.G. Magalhaes, C. Garner, M. De Waard, S. Amigorena, A. Feltz, J.-M. Mallet, M. Collot, H-Rubies, A new family of red emitting fluorescent pH sensors for living cells, Chem. Sci. 6 (2015) 5928–5937, https://doi.org/10.1039/C5SC01113B.
[38] C. Kembuan, H. Oliveira, C. Graf, Effect of different silica coatings on the toxicity of upconversion nanoparticles on RAW 264.7 macrophage cells, Beilstein J. Nanotechnol. 12 (2021) 35–48, https://doi.org/10.3762/bjnano.12.3.